Topological Transitions Induced by Antiferromagnetism in a Thin-Film Topological Insulator

Qing Lin He,[1,2,*] Gen Yin,[1] Luyan Yu,[1] Alexander J. Grutter,[3] Lei Pan,[1] Chui-Zhen Chen,[4] Xiaoyu Che,[1] Guoqiang Yu,[1] Bin Zhang,[5] Qiming Shao,[1] Alexander L. Stern,[6] Brian Casas,[6] Jing Xia,[6] Xiaodong Han,[5] Brian J. Kirby,[3] Roger K. Lake,[7] K. T. Law,[4] and Kang L. Wang[1,†]

[1]*Department of Electrical Engineering, University of California, Los Angeles, California 90095, USA*
[2]*International Center for Quantum Materials, Peking University, Beijing 100871, China*
[3]*NIST Center for Neutron Research, National Institute of Standards and Technology, Gaithersburg, Maryland 20899-6102, USA*
[4]*Department of Physics, Hong Kong University of Science and Technology, Clear Water Bay, Hong Kong, China*
[5]*Beijing Key Lab of Microstructure and Property of Advanced Materials, Beijing University of Technology, 100124, Beijing, China*
[6]*Department of Physics and Astronomy, University of California, Irvine, California 92697, USA*
[7]*Laboratory for Terascale and Terahertz Electronics (LATTE), Department of Electrical and Computer Engineering, University of California, Riverside, Riverside, California 92521, USA*

(Received 25 January 2018; published 29 August 2018)

Magnetism in topological insulators (TIs) opens a topologically nontrivial exchange band gap, providing an exciting platform for manipulating the topological order through an external magnetic field. Here, we show that the surface of an antiferromagnetic thin film can magnetize the top and the bottom TI surface states through interfacial couplings. During the magnetization reversal, intermediate spin configurations are ascribed from unsynchronized magnetic switchings. This unsynchronized switching develops antisymmetric magnetoresistance spikes during magnetization reversals, which might originate from a series of topological transitions. With the high Néel ordering temperature provided by the antiferromagnetic layers, the signature of the induced topological transition persists up to ~90 K.

DOI: 10.1103/PhysRevLett.121.096802

Currently there is immense interest in the manipulation of ferromagnetic phases in topological insulators (TIs) through either doping with magnetic elements or proximity coupling to a strong ferromagnetic system. This interest is driven by the novel physics which is a consequence of the nontrivial topology in k space [1–7]. Breaking time-reversal symmetry in these systems with magnetic dopants such as Cr or V opens an exchange band gap, inducing a finite Berry curvature and leading to an intrinsic anomalous Hall effect (AHE) [8,9]. Inside this exchange gap, nonzero Chern numbers of ± 1 arise, protecting a chiral edge mode which encircles the boundary of the TI thin film [1–3,10]. Similar to the edge mode in a quantum Hall effect, backscattering is forbidden in the chiral mode, enabling dissipationless charge transport. Other than doping, proximity coupling to ferromagnets is another common method to introduce ferromagnetic order in TIs. Since the magnetic order in this case is introduced extrinsically by an adjacent ferromagnetic layer with a high T_C, it can persist at much higher temperatures than that induced by magnetic doping [11–13].

Besides ferromagnets, antiferromagnets (AFMs) have been recently shown to enhance the magnetic order of a Cr doped TI thin film through interfacial exchange coupling [14]. AFMs have vanishingly small net magnetization and consequently neither produce stray fields nor affect the characterization of the TI layer. Therefore, the magnetic order is robust against the external magnetic field or moderate current perturbations, minimizing the crosstalk between devices and improving the scalability [15]. In this Letter, we experimentally demonstrate the manipulation of topological orders and the transport behavior in an intrinsic TI thin film *in situ* grown on top of (or sandwiched between) antiferromagnetic CrSb thin films. In CrSb (NiAs phase), Cr spins lie along the c axis, exhibiting a layered antiferromagnetic order with spins aligned ferromagnetically within the basal plane and antiferromagnetically between adjacent planes. Such a magnetic structure can induce uncompensated spins at the AFM/TI interface, resulting in a short-range interfacial exchange coupling experienced by TI surface states [16]. A similar exchange coupling can also originate from the remanence net magnetization due to defects or surface roughness. This interfacial exchange coupling magnetizes the surface Dirac fermions in the TI, giving rise to an observed AHE that survives up to 90 K. More importantly, we observed that the magnetizations of the top and the bottom TI surfaces can switch in a step-by-step manner. As a result, two antisymmetric magnetoresistance (MR) spikes show up during the sweep of the magnetic field. These two spikes may correspond to different magnetic configurations, representing two distinct topological orders.

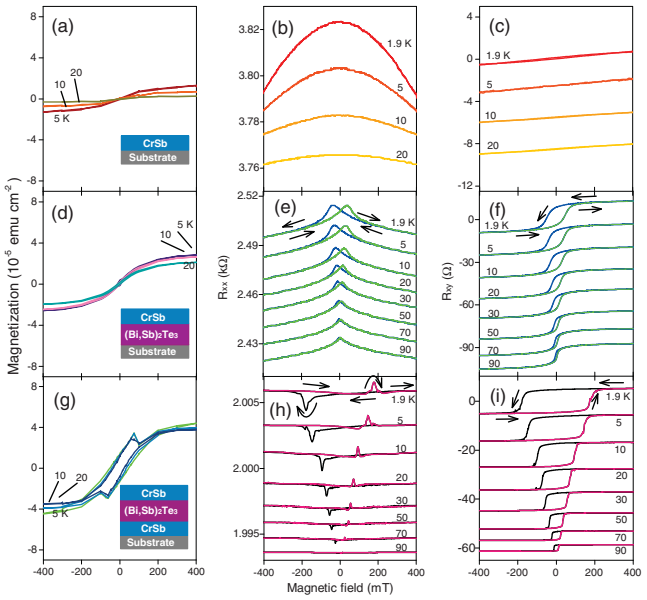

FIG. 1. (a) Temperature-dependent M-H loops of a 12 nm AFM thin film, CrSb, grown on a GaAs substrate, which exhibits negligible magnetization. (b) and (c) show the results of the longitudinal (R_{xx}) and the Hall (R_{xy}) resistances, respectively. The absence of hysteresis in both measurement results, i.e., the small parabolic curvature in R_{xx} and the linear response in R_{xy}, suggests that the CrSb layer does not generate an AHE intrinsically. (d)–(f) show the corresponding results of an AFM/TI bilayer, demonstrating the transport signature of the top-surface magnetization of the TI layer. (g)–(i) are from an AFM/TI/AFM trilayer, in which an antisymmetric MR behavior and an AHE are observed. Traces are offset for clarity, except for the traces at 1.9 K in (b), (c), (e), (f), (h), and (i). (1 μemu = 1 nA m^2)

First, in order to ascertain the magnetic order in CrSb thin films, superconducting quantum interference device magnetometry and magnetotransport measurements were carried out on a 12 nm CrSb layer grown on a GaAs substrate. The grown CrSb is in the antiferromagnetic NiAs phase rather than the ferromagnetic zinc-blende phase, which was confirmed by the XRD pattern (Supplemental Material [17]). An external magnetic field was applied perpendicularly to the film plane. As shown in Fig. 1(a), a vanishingly weak magnetization is captured in the M-H measurement, diminishing quickly as the temperature increases to ~20 K. Such an M-H loop is para- or superparamagnetic-like, which may originate from puddles of uncompensated spins in the AFM layer, either inside the bulk or at the interface, or both [14,16]. Consistently, magnetotransport measurements also capture a small negative MR which also vanishes at around 20 K [Fig. 1(b)]. The corresponding Hall resistance obtained [Fig. 1(c)] in a 2 mm × 1 mm Hall bar varies linearly with the external field, indicating that the Hall signal is mainly associated with the ordinary Hall effect. These results suggest that the weak magnetization in the CrSb thin film results in neither magnetic hysteresis nor intrinsic AHE.

When the AFM layer was epitaxially grown on a 8-nm TI thin film, an induced AHE was observed. As shown in Fig. 1(d), the saturation magnetization is roughly 3×10^{-5} emu cm^{-2}, which is higher than that of the single AFM layer grown on the substrate [Fig. 1(a)]. This small magnetization should be determined by the interfacial details. Some uncompensated spins on the surface of a thin-film CrSb are likely to occur due to lattice mismatch [18–20], atomic steps [21], or defects. When these surface spins are not fully compensated by their antiparallel counterparts, a net surface magnetization of CrSb can be experienced by the TI surface state due to the interfacial wave-function overlap. This opens an exchange band gap, resulting in an observable AHE. To explore this mechanism, transport measurements were carried out using this bilayer sample with the results summarized in Figs. 1(e) and 1(f). This MR measurement exhibits a hysteretic butterfly shape which gradually vanishes as the temperature increases to 90 K, as shown in Fig. 1(e). The corresponding Hall resistance loops at different temperatures are shown in Fig. 1(f). Note that the AHE signal is evidenced by a large hysteresis even without subtracting the linear ordinary Hall resistance, indicating a strong induced magnetic order in the AFM/TI bilayer. Such an order is not likely caused by the accidental Cr diffusion from the CrSb layer into the TI layer, which is supported by two control samples: one is a heavily Cr-doped TI layer with the Cr-source temperature the same as that to grow the CrSb, while the other is a Cr layer deposited on top of a TI layer that is fabricated under the same growth condition of the CrSb/TI heterostructure. The AHE in the first sample disappears at 50 K (Supplemental Material, Fig. S3), while the second one does not show signature of AHE, which implies that the Cr diffusion is negligible in the growth condition of the heterostructures and could not be the cause of the observed effect. To investigate the effects of lattice mismatch in the AFM/TI/substrate growth order, another growth order of TI/AFM/substrate is also examined. A similar induced AHE can be observed with both growth orders (Supplemental Material, Fig. S4), suggesting that the lattice mismatch is not the reason for the observed magnetotransport behavior. This also suggests that both the top and the bottom surfaces of the TI layer can be magnetized through interfacial couplings.

Strikingly, when introducing one additional AFM layer to form an AFM/TI/AFM sandwich structure, a distinctly different MR behavior is revealed. In contrast to Figs. 1(a) and 1(d), the M-H results show clear hysteresis loops from 5 to 20 K [Fig. 1(g)], which implies the presence of unsynchronized switching of the magnetizations at the top and the bottom interfaces. Because of the details of these interfaces, such as roughness and defects, the coercivities of the top and the bottom interfaces are expected to vary, inducing a step-by-step switching behavior. Corresponding to this double switching, the temperature-dependent MR shows antisymmetric spikes during the magnetization

reversals, as shown in Fig. 1(h). These spikes occur when the corresponding AHE resistance changes sign [Fig. 1(i)]. This antisymmetric MR contrasts sharply with the symmetric MR observed in most ferromagnetic systems [11], as well as the case of the AFM/TI bilayer in this work. The antisymmetric behavior also survives up to ~90 K, which again underscores the importance of the high magnetic ordering temperature provided by the CrSb layers. Here, we propose that the observed antisymmetric MR of the AFM/TI/AFM trilayer has a surprising origin—an intermediate topological order during the double-switching process, as discussed below.

Recently, it was experimentally demonstrated that an axion insulator phase can show up when the surface magnetizations of a TI thin film are opposite [22–24]. Here, we demonstrate that when the surface magnetizations reverse in a particular unsynchronized manner, a series of topological phase transitions could happen due to the competition between the hybridization gap and the exchange gap. This results in the antisymmetric MR behavior as observed in our experiment. The surface magnetization of the AFM/TI/AFM trilayer can be described by Eq. (1), where an effective Hamiltonian of a thin-film TI [25] is sandwiched between two CrSb layers:

$$H(\mathbf{k}) = \begin{bmatrix} h_0(\mathbf{k}) & t & 0 & 0 \\ t^\dagger & h_T(\mathbf{k}) & m_k & 0 \\ 0 & m_k & h_B(\mathbf{k}) & t \\ 0 & 0 & t^\dagger & h_0(\mathbf{k}) \end{bmatrix}. \quad (1)$$

Here, $h_{T,B}(\mathbf{k}) = \pm\hbar v_F(\sigma_x k_y - \sigma_y k_x) + M_{T,B}\sigma_z$, denoting the top and the bottom surfaces of a TI thin film, while $h_0 = (\hbar^2 k^2/m_0)\mathbf{I}_{2\times 2}$, representing the conducting channels in the top and the bottom CrSb layers, respectively. A weak coupling term (t) describes the hopping between the CrSb layers and the TI surfaces. $m_k = m_0 - m_1 k^2$ is the parabolic component induced by the surface-to-surface coupling ($m_0 > 0$). Here "T" and "B" label the top and the bottom surfaces whereas v_F is the Fermi velocity of the surface Dirac fermions [26,27]. Because of the surface magnetization, a Hund's-rule exchange coupling term, $M_{T,B}$, is introduced to break the time-reversal symmetry. When the magnetization experienced by the surface state switches, $M_{T,B}$ changes sign. To describe the magnetoelectric transport behavior, we establish a tight-binding model by discretizing $k_\alpha \to -i\partial_\alpha$ with a finite grid size a. The band structure of a thin film can be obtained using this tight-binding model with different magnetic configurations, as shown in Figs. 2(a)–2(d). k_y is quantized into subbands due to the finite size. When M_T and M_B have the same sign and are larger than the hybridization gap m_0 (cases i and iii), $C = \pm 1$, and chiral edge modes are therefore introduced as depicted by Figs. 2(a) and 2(c). The magnetic TI thin film Hamiltonian (excluding the h_0 terms) can describe

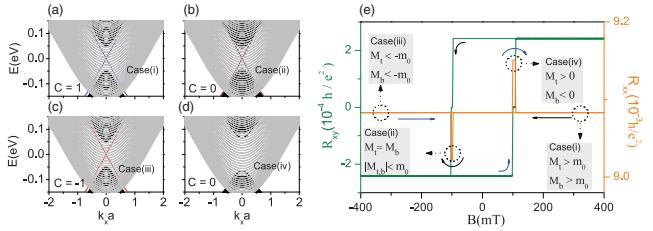

FIG. 2. (a)–(d) The black solid lines show the energy spectrum of a TI thin film with different top-bottom spin configurations. The grey lines indicate the parabolic bands from the AFM layers. The system has a periodic boundary condition in the x direction and open boundary conditions in the y direction. (a)–(d) The energy spectrum from case (i) to case (iv), respectively. The grey lines show the parabolic bands given by the CrSb layers, while the black solid lines demonstrate the TI surface bands. (e) The evolution of the longitudinal resistance R_{xx} and the Hall resistance R_{xy} during the unsynchronized magnetic switching. The solid black arrows and the blue arrows denote the positive-to-negative and negative-to-positive field scan, respectively.

a quantum-anomalous-Hall (QAH) phase with $C = \pm 1$ counting the number of topologically protected edge modes [25,28,29]. On the other hand, during the reversal of the magnetization, unsynchronized switching may occur, inducing intermediate magnetic configurations without edge modes. When $M_T > 0$ and $M_B < 0$, the edge modes are gapped out due to the breaking of both time-reversal symmetry and inversion symmetry (case iv), and an insulating phase is therefore obtained [Fig. 2(d)]. Interestingly, during the reversal of the magnetization, an intermediate magnetic configuration can occur as shown by case (ii). In this case, the $C = 0$ Chern number can possess counterpropagating edge modes induced by a restored inversion symmetry when both $M_T = M_B$ and $|M_{T,B}| < m_0$ are satisfied in a transient spin configuration. The energy spectrum of this special case is depicted in Fig. 2(b).

It is important to note that the different $M_{T,B}$ configurations can be detected by measuring the longitudinal (R_{xx}) and the Hall resistance (R_{xy}) as demonstrated in Fig. 2(e), in which, R_{xx} and R_{xy} of the magnetic thin film and the antiferromagnetic layers are calculated numerically using nonequilibrium Green's function techniques (see Supplemental Material for details [17]) [30,31]. In an ideal QAH phase with Chern number $C = \pm 1$, it is expected that R_{xx} vanishes and R_{xy} is quantized to h/e^2. In the present material system, due to the conducting channels in the AFM layers, R_{xx} and R_{xy} deviate from the expected values. This behavior is qualitatively captured in Fig. 2(e) (cases i and iii). Importantly, when $M_T = M_B$ and $|M_{T,B}| < m_0$, two counterpropagating helical edge modes arise due to the restored inversion symmetry of the sandwich structure, and R_{xx} is therefore reduced (case ii). On the other hand, when M_T and M_B have opposite signs, the edge channels are absent and R_{xx} is increased (case iv). Because of the intrinsic asymmetry of M_T and M_B, we obtain antisymmetric

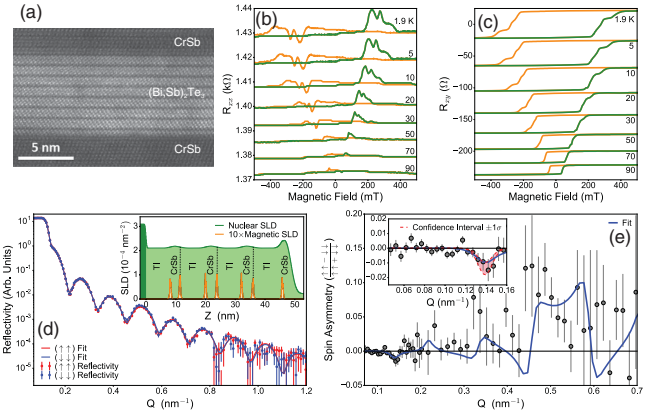

FIG. 3. (a) A cross-sectional scanning transmission electron microscope image obtained from a superlattice, which captures the sharp interfaces between the TI layer sandwiched by two AFM layers. There is a small in-plane rotation between the top and the bottom CrSb layers when interfacing with TI surfaces; i.e., the top AFM layer is taken along the $(1\bar{2}10)$ zone axis while the bottom one slightly deviates from it. (b),(c) R_{xx} and R_{xy} results of the superlattice as functions of external perpendicular magnetic fields at different temperatures, respectively. (d) Neutron reflectivity for the spin-polarized $R_{\uparrow\uparrow}$ and $R_{\downarrow\downarrow}$ channels of the SL along with (e), spin asymmetry (at 6 K with a 700 mT in-plane field). The inset in (d) shows the corresponding model with structural and magnetic scattering length densities (SLDs) used to obtain the best fit. The error bars are ± 1 standard deviation. The inset in (e) exhibits the first dip right after the critical edge.

magnetoresistance (R_{xx}) spikes during magnetization reversals as demonstrated in Fig. 2(e). It is remarkable that the experimentally measured R_{xx} and R_{xy} in Figs. 1(h) and 1(i) can be well explained by the numerical simulations, where the observation of the negative R_{xx} spike indicates the presence of the phase with counterpropagating edge modes, whereas the step structure of R_{xy} indicates the observation of the $C = \pm 1$ phase. Since the antisymmetric R_{xx} and the step structure of R_{xy} are observable experimentally at 90 K, we conclude that the topological phases in our AFM/TI/AFM trilayer can survive to 90 K.

Following the topological transition model described above, it is expected that the induced AHE and the antisymmetric MR features will become more pronounced in an $(\mathrm{AFM/TI})_n$ (n is defined as the repeating number of the AFM/TI bilayer) superlattice structure. To confirm this scenario, we prepared a high-quality superlattice of $n = 4$ [Fig. 3(a)], and performed similar temperature-dependent magnetotransport measurements. As expected, even stronger antisymmetric MR and AHE signals are present. Furthermore, multiple spikes are observed in the MR loops during the magnetization reversal, which again coincide with the multiple Hall-resistance steps near the coercivities. Similar to the AFM/TI/AFM trilayer case, these features likely indicate the unsynchronized switchings of different interfacial channels. The multiple-switching behavior may stem from larger variations in the switching fields due to the increased number of slightly different AFM/TI interfaces. Figures 3(b) and 3(c) provide further experimental evidence that the magnetization reversal process occurs in a step-by-step manner in such a superlattice structure. Note that this set of multiple antisymmetric MR behaviors is different from the one induced by domain structures [32] since the antisymmetric polarity does not change with the measurement configuration. Details can be found in Sec. VIII of the Supplemental Material [17].

To quantitatively investigate the net magnetic polarization with detailed depth-dependent information, we probed a representative $n = 4$ superlattice using polarized neutron reflectometry (PNR). PNR was performed at 6 K in an applied in-plane magnetic field of 700 mT. The non-spin-flip specular reflectivities, sensitive to the depth profile of the nuclear scattering length density and the net in-plane magnetization, were measured as a function of the momentum transfer vector Q_Z. Figure 3(d) shows the fitted reflectivities alongside the most likely nuclear and magnetic depth profiles, while the magnetic features may be more clearly seen in the spin asymmetry ratio (defined as the difference between the two non-spin-flip reflectivities normalized by their sum) plotted in Fig. 3(e). In this figure, with the spin asymmetry, we observe small but nonzero splitting (a small dip shown in the inset) between the reflectivities near the critical edge ($Q_Z = 0.15\ \mathrm{nm}^{-1}$) and at the first-order superlattice reflection ($Q_Z = 0.45$–$0.6\ \mathrm{nm}^{-1}$).

The magnetic profile of the superlattice is extracted by comparing several fitting models which may describe the data. The best physically reasonable solution, shown in the inset of Fig. 3(d), exhibits a net magnetization at the AFM/TI interfaces (model 1 in the Supplemental Material [17]). In this model, the interface possesses a net magnetization of approximately 30 emu cm^{-3}. Although the resulting magnetization is weak, the statistical significances of each two features are 3.3 and 5.75 standard deviations, respectively. See the Supplemental Material for more details of the statistical analysis, using methods described in Refs. [33–35]. We note that the PNR data can also be described by alternative models. However, most of these models (models 3–6) either fail to precisely capture the splitting near the critical edge, or they cannot represent the first-order superlattice reflection. One of the alternative models (model 2) assumes that uniform ferromagnetic order may occur both in the antiferromagnetic CrSb layers and the TI layers with different magnitudes, which can capture both features reasonably well. However, based on the XRD result, CrSb layers are in the antiferromagnetic NiAs phase, rather than the ferromagnetic zinc-blende phase, so that the net magnetization should be zero in the bulk. Also, since the TI layers are not magnetically doped, it is not physically plausible to assume that ferromagnetic order can exist uniformly in the TI layers. As a result, this model is also eliminated from

consideration. With that, we conclude that a modulated magnetic depth profile should be present, with the magnetization mainly distributed at the interfaces. Here, we point out that the PNR result cannot fully resolve the magnetic profile at the atomic level. The observed peaks in the depth profile could be induced by (i) the uniform frontmost Cr layer on the AFM side, (ii) the uncompensated spins at the interface due to defects or surface roughness, or (iii) by the induced local magnetic moments on the TI side. All these cases could induce the transport signatures observed in our experiments due to the electron-wave overlap between the surface carriers and the local moments.

This work was supported as part of the SHINES Center, an Energy Frontier Research Center (EFRC) funded by the U.S. Department of Energy (DOE), Office of Science, Basic Energy Sciences under Award No. S000686. Q. L. He acknowledges the supports from the National Natural Science Foundation of China (Grant No. 11874070), the National Key R&D Program of China (Grant No. 2018YFA0305601), and National Thousand-Young-Talents Program in China. We are also grateful for the support from the National Science Foundation (DMR-1411085), and the ARO program under Contract No. W911NF-15-1-10561. K. T. Law acknowledges the support of Hong Kong Research Grants Council (HKRGC) through C6026-16W, the Croucher Foundation, and the Tai-chin Lo Foundation. This work used the Extreme Science and Engineering Discovery Environment (XSEDE), which is supported by National Science Foundation Grant No. OCI-1053575. Specifically, it used the Bridges system, which is supported by NSF Grant No. ACI-1445606, at the Pittsburgh Supercomputing Center (PSC).

Q.-L. H., G. Y., and L. Y. contributed equally to this work.

*Corresponding author.
qlhe@pku.edu.cn
†Corresponding author.
wang@ee.ucla.edu

[1] C.-Z. Chang *et al.*, Science **340**, 167 (2013).
[2] X. Kou *et al.*, Phys. Rev. Lett. **113**, 137201 (2014).
[3] R. Yu, W. Zhang, H.-J. Zhang, S.-C. Zhang, X. Dai, and Z. Fang, Science **329**, 61 (2010).
[4] X.-L. Qi and S.-C. Zhang, Rev. Mod. Phys. **83**, 1057 (2011).
[5] C. L. Kane and E. J. Mele, Phys. Rev. Lett. **95**, 146802 (2005).
[6] H. Zhang, C.-X. Liu, X.-L. Qi, X. Dai, Z. Fang, and S.-C. Zhang, Nat. Phys., **5**, 438 (2009).
[7] B. A. Bernevig, T. L. Hughes, and S.-C. Zhang, Science **314**, 1757 (2006).
[8] N. Nagaosa, J. Sinova, S. Onoda, A. H. MacDonald, and N. P. Ong, Rev. Mod. Phys. **82**, 1539 (2010).
[9] D. Xiao, M.-C. Chang, and Q. Niu, Rev. Mod. Phys. **82**, 1959 (2010).
[10] C.-Z. Chang, W. Zhao, D. Y. Kim, H. Zhang, B. A. Assaf, D. Heiman, S.-C. Zhang, C. Liu, M. H. W. Chan, and J. S. Moodera, Nat. Mater. **14**, 473 (2015).
[11] M. Lang *et al.*, Nano Lett. **14**, 3459 (2014).
[12] Z. Jiang, C.-Z. Chang, C. Tang, P. Wei, J. S. Moodera, and J. Shi, Nano Lett. **15**, 5835 (2015).
[13] F. Katmis *et al.*, Nature (London) **533**, 513 (2016).
[14] Q. L. He *et al.*, Nat. Mater. **16**, 94 (2017).
[15] T. Jungwirth, X. Marti, P. Wadley, and J. Wunderlich, Nat. Nanotechnol. **11**, 231 (2016).
[16] W. Luo and X.-L. Qi, Phys. Rev. B **87**, 085431 (2013).
[17] See Supplemental Material at http://link.aps.org/supplemental/10.1103/PhysRevLett.121.096802 for details about the film growth, nonequilibrium Green's function calculation, polarized neutron reflectrometry, structural characterizations, discussion of diffusion, and additional transport measurements.
[18] A. I. Snow, Rev. Mod. Phys. **25**, 127 (1953).
[19] B. T. M. Willis, Acta Cryst. **6**, 425 (1953).
[20] T. Kaneko, H. Yoshida, M. Ohashi, S. Abe, and K. Kamigaki, J. Phys. Soc. Jpn. **37**, 1465 (1974).
[21] H. Dohnomae, K. Shintaku, N. Nakayama, and T. Shinjo, J. Magn. Magn. Mater. **126**, 346 (1993).
[22] M. Mogi, M. Kawamura, R. Yoshimi, A. Tsukazaki, Y. Kozuka, N. Shirakawa, K. S. Takahashi, M. Kawasaki, and Y. Tokura, Nat. Mater. **16**, 516 (2017).
[23] M. Mogi, M. Kawamura, A. Tsukazaki, R. Yoshimi, K. S. Takahashi, M. Kawasaki, and Y. Tokura, Sci. Adv. **3**, eaao1669 (2017).
[24] D. Xiao *et al.*, Phys. Rev. Lett. **120**, 056801 (2018).
[25] W.-Y. Shan, H.-Z. Lu, and S.-Q. Shen, New J. Phys. **12**, 043048 (2010).
[26] H.-Z. Lu, A. Zhao, and S.-Q. Shen, Phys. Rev. Lett. **111**, 146802 (2013).
[27] H.-Z. Lu, W.-Y. Shan, W. Yao, Q. Niu, and S.-Q. Shen, Phys. Rev. B **81**, 115407 (2010).
[28] X.-L. Qi, T. L. Hughes, and S.-C. Zhang, Phys. Rev. B **82**, 184516 (2010).
[29] F. D. M. Haldane, Phys. Rev. Lett. **61**, 2015 (1988).
[30] S. Datta, *Quantum Transport: Atom to Transistor* (Cambridge University Press, Cambridge, England; New York, 2005), 2nd ed., .
[31] R. Lake, G. Klimeck, R. C. Bowen, and D. Jovanovic, J. Appl. Phys. **81**, 7845 (1997).
[32] X. M. Cheng, S. Urazhdin, O. Tchernyshyov, C. L. Chien, V. I. Nikitenko, A. J. Shapiro, and R. D. Shull, Phys. Rev. Lett. **94**, 017203 (2005).
[33] P. A. Kienzle, J. Krycka, N. Patel, and I. Sahin, *Bumps (Version 0.7.5.4) [Computer Software]. College Park, MD: University of Maryland* (University of Maryland, College Park, MD, 2011).
[34] B. J. Kirby, P. A. Kienzle, B. B. Maranville, N. F. Berk, J. Krycka, F. Heinrich, and C. F. Majkrzak, Current Opinion in Colloid & Interface Science **17**, 44 (2012).
[35] J. Towns *et al.*, Comput. Sci. Engin. **16**, 62 (2014).